FIRST-PRINCIPLES INVESTIGATION OF

ELECTRONIC PROPERTIES IN SODIUM-ION ELECTROLYTES FOR SOLID-STATE

BATTERY MATERIALS

BY

LARRY E. RUSH JR.

A Thesis Submitted to the Graduate Faculty of

WAKE FOREST UNIVERSITY GRADUATE SCHOOL OF ARTS AND SCIENCES

in Partial Fulfillment of the Requirements

for the Degree of

MASTER OF SCIENCE

Physics

May 2017

Winston-Salem, North Carolina

Approved By:

Natalie Holzwarth, Ph.D., Advisor

Martin Guthold, Ph.D., Chair

Grey Ballard, Ph.D.

Table of Contents

List of Figures

Abstract

This thesis mainly focuses on characterizing and understanding the electronic properties of sodium-ion electrolytes using first-principles calculations. The core of these calculations is built upon a functional understanding of the relationship between quantum mechanics and the crystalline geometries that contribute to unique properties of materials such as diffusion mechanisms of ions within solid-state materials, conductivity, and ground state structures. The goal of this body of work is to understand how this relationship can give us insight into materials that might have use in an emerging field within battery technology. Sodium-ion solid-state batteries are an auspicious technology because nature has provided us with widely distributed precursor materials in such a way that removes geopolitical constraints in its construction and distribution. This is extremely important to individuals (and a collection of individuals) who want to expedite the wide use of clean and renewable energy from a societal perspective. An example is Morocco's initiative to generate 52% of its total energy consumption from clean and renewable energy sources to eliminate dependencies on foreign countries to supply energy resources[1]. Sodium-ion solid-state batteries are an inexpensive option for large-scale grid storage, so this could play a role in providing a cost-effective option for Morocco. The challenging part is to sift through the large chemical space of sodium-ion solid-state electrolytes to find optimal materials for battery technology, and that is what motivates this body of work.

Chapter 1

Introduction

Storing energy and converting it to something useful has been a difficult problem for humanity, especially when one adds additional constraints such as solving this issue in a safe and cost-effective manner (e.g. Samsung's explosive battery issue[2]). Batteries are an important component for solving our societal energy demands because they are able to convert electrochemical energy to electrical energy in a way that allows us to take advantage of its portability and effectiveness for off-grid usage. Lithium-ion solid-state batteries are widely used in numerous industries including automotive (e.g. Tesla's electric vehicles and the Los Angeles Police Department's stealthy electric motorcycles), portable electronics, medical devices, and so forth. However, lithium has the drawback of being expensive, it has the need to be protected from over-charging during the charge/discharge cycle, and lithium-ion batteries have to be transported in a restricted manner due to the lack of air-stability within the material; therefore, the demand for seeking an alternative to lithium-ion batteries has increased.

Sodium-ion solid-state batteries are ideal candidates for replacements of its lithium counterparts because sodium lies in the same group on the periodic table as lithium, it has similar chemical properties to lithium, and sodium is much more abundant than lithium, which makes it a cost-effective and geopolitically-neutral alternative. Another important feature for sodium-ion battery materials is the fact that the sodium ions seem to have higher intercalation than lithium ions, meaning that sodium ions are able to reversibly seep through layers within the electrodes better than lithium ions during the charge/discharge cycle[3]. This work, however, will further explore the boundaries for sodium-ion containing

electrolytes as battery materials by investigating the interface properties of Na_3SbS_4 with metallic sodium, in order to simulate the electronic effects that occur when the anode comes in contact with the electrolyte. Furthermore, this work will illuminate a structural puzzle between $Na_4P_2S_6$ and $Li_4P_2S_6$, to expand on the electronic differences between sodium-ion solid-state electrolytes and lithium-ion solid-state electrolytes in battery materials.

Chapter 2

Methods

Density Functional Theory (DFT) is the basis on which all calculations in this work was built. DFT is an approximation to the many-body problem by mapping the exact ground-state many-electron wavefunction to a more manageable wavefunction that solves for a ground-state one-body electron density. In order to understand how this is done, consider the following[4]:

The many-body Hamiltonian can be written as:

$$H = H_{int} + V_{ext}. \tag{2.1}$$

H_{int} is the kinetic energy of the electrons plus electron-electron Coulomb interactions:

$$H_{int} = \sum_i \frac{p_i^2}{2m} + \frac{1}{2} \sum_{i \neq j} \frac{e^2}{|r_i - r_j|} \tag{2.2}$$

where p_i is the momentum of each electron, r_i and r_j are the positions of the ith and jth electron from the origin. V_{ext} is a single particle interaction

$$V_{ext} = \sum_i v_{ext}(r_i), \tag{2.3}$$

which is naturally chosen as the electron-nuclear interaction:

$$v_{ext}(r) \equiv V_{nucl}(r) = \sum_I -\frac{Z_I e^2}{|r - R_I|}. \tag{2.4}$$

Here R_I is the position of the Ith nucleus and Z_I is its atomic number.

If we suppose that for a given system with a ground-state many-body non-degenerate wavefunction $|\psi_G\rangle$ where v_{ext} is fixed, the Hohenberg-Kohn theorem states that there is a

one-to-one correspondence between the ground-state density of a N-electron system and v_{ext}. This means that the ground-state electron density becomes the variable of interest. Since the ground-state wavefunction depends on a given external potential, it can be written as $\psi_G[v_{ext}]$, which makes it a functional (meaning that ψ is a function of a function). The electron density for N particles is defined as:

$$n(r) = \langle \psi_G(r_1, r_2, ..., r_N)| \sum_i \delta(r - r_i) |\psi_G(r_1, r_2, ..., r_N)\rangle \tag{2.5}$$

If we multiply $n(r)$ by v_{ext} and integrate over all space, we get:

$$\int_{all-space} \langle \psi_G(r_1, r_2, ..., r_N)| \sum_i \delta(r - r_i)v_{ext}(r_i) |\psi_G(r_1, r_2, ..., r_N)\rangle \, d^3r \tag{2.6}$$

which is

$$\langle \psi_G(r_1, r_2, ..., r_N)| V_{ext} |\psi_G(r_1, r_2, ..., r_N)\rangle \tag{2.7}$$

Since the wavefunction is a functional of the external potential, this implies that $n(r)$ is equal to some functional, $F[v_{ext}]$, which foundationally leads to $v_{ext} = F^{-1}[n(r)] = G[n(r)]$. This is novel because knowledge of the ground-state density, $n(r)$, can determine uniquely the external potential of the system or vice versa (and thus the Hamiltonian which keeps track of all interactions in the system to give us knowledge about the properties of a system).

To prove this, let us consider two external potentials, $v_{ext}(r)$ and $\bar{v}_{ext}(r)$, such that $v_{ext}(r) \neq \bar{v}_{ext}(r)$ which implies $n(r) \neq \bar{n}(r)$. If we wanted to describe these systems with the corresponding Hamiltonians, H and $\bar{H}$, this would lead to $H = H_{int} + V_{ext}$ and $\bar{H} = H_{int} + \bar{V}_{ext}$. If we were to consider the eigenvalues E_G and $\bar{E}_G$ for the ground-state wavefunctions $|\psi_G\rangle$ and $|\bar{\psi}_G\rangle$, we have:

$$\langle \bar{\psi}_G| H |\bar{\psi}_G\rangle = \langle \bar{\psi}_G| H_{int} + V_{ext} + \bar{V}_{ext} - \bar{V}_{ext} |\bar{\psi}_G\rangle \tag{2.8}$$

$$= \langle \bar{\psi}_G| H_{int} + \bar{V}_{ext} |\bar{\psi}_G\rangle + \langle \bar{\psi}_G| V_{ext} - \bar{V}_{ext} |\bar{\psi}_G\rangle \tag{2.9}$$

$$\Rightarrow \langle \bar{\psi}_G| H_{int} + V_{ext} |\bar{\psi}_G\rangle = \bar{E}_G + \int \bar{n}(r)[v_{ext} - \bar{v}_{ext}]d^3r \tag{2.10}$$

Since ground-state eigenvalue of H is strictly lower than the mean value of the Hamultonian in any other state (i.e. the Variational Principle), equation 2.10 becomes:

$$\langle \psi_G| H_{int} + V_{ext} |\psi_G\rangle < \langle \bar{\psi}_G| H_{int} + V_{ext} |\bar{\psi}_G\rangle \tag{2.11}$$

$$\Rightarrow E_G < \bar{E}_G + \int \bar{n}(r)[v_{ext}(r) - \bar{v}_{ext}(r)]d^3r \tag{2.12}$$

Similarly, if one were to examine $\langle \psi_G | \bar{H} | \psi_G \rangle$, one would find the eigenvalue of $\bar{H}$ to be:

$$\bar{E}_G < E_G + \int n(r)[\bar{v}_{ext}(r) - v_{ext}(r)]d^3r \tag{2.13}$$

If you take the assumption that $n(r) = \bar{n}(r)$, then $v_{ext}(r) = \bar{v}_{ext}(r)$ and thus equations 2.12 and 2.13 are contradictory statements. Therefore, we must impose that the electron densities and consequently the external potentials must not be equal, thus proving uniqueness.

Therefore, if we want to write the energy of the system as a function of electron density, Hohenberg-Kohn theorem states

$$E[n(r); v_{ext}(r)] = T[n(r)] + E_{ee}[n(r)] + \int v_{ext}(r)n(r)d^3r, \tag{2.14}$$

where

$$T[n] = \langle \psi_G | \sum_i \frac{p_i^2}{2m} | \psi_G \rangle \tag{2.15}$$

and

$$E_{ee}[n] = \langle \psi_G | \frac{1}{2} \sum_{i \neq j} \frac{e^2}{|r_i - r_j|} | \psi_G \rangle . \tag{2.16}$$

The minimum of this energy will give us the exact ground-state energy for the many-body system. If the functional,

$$F[n(r)] = T[n(r)] + E_{ee}[n(r)], \tag{2.17}$$

which does not depend on $v_{ext}(r)$ was known explicitly, we could just take the functional derivative with respect to the density to find the ground-state. In reality, $F[n(r)]$ is not known explicitly so it must be approximated. I will refer to the ground-state energy of sodium-ion solid-state electrolytes, and this is how the software that I ran calculated the ground-state for the system. Before I go further, let us consider what a functional derivative is by considering the action integral in the principle of least action in physics:

$$A = \int_{t_1}^{t_2} L(x(t), \dot{x}(t), t)dt \tag{2.18}$$

Where L is the Lagrangian that is a function of the coordinate $x(t)$, velocity $\dot{x}(t)$, and time. If we consider the variation of A:

$$\delta A = \int_{t_1}^{t_2} (\frac{\partial L}{\partial x}\delta x + \frac{\partial L}{\partial \dot{x}}\delta \dot{x})dt \tag{2.19}$$

explicit t dependence goes away since t is an independent variable (meaning it is not a function). We know from the product rule that:

$$\frac{d}{dt}(\frac{\partial L}{\partial \dot{x}}\delta x) = \frac{d}{dt}(\frac{\partial L}{\partial \dot{x}})\delta x + \frac{\partial L}{\partial \dot{x}}\delta \dot{x} \tag{2.20}$$

$$\Rightarrow \frac{\partial L}{\partial \dot{x}}\delta \dot{x} = \frac{d}{dt}(\frac{\partial L}{\partial \dot{x}}\delta x) - \frac{d}{dt}(\frac{\partial L}{\partial \dot{x}})\delta x \tag{2.21}$$

We can substitute equation 2.15 into equation 2.13 and separate the integrals such that:

$$\delta A = \int_{t_1}^{t_2} \frac{d}{dt}(\frac{\partial L}{\partial \dot{x}}\delta x)dt + \int_{t_1}^{t_2}(\frac{\partial L}{\partial x} - \frac{d}{dt}\frac{\partial L}{\partial \dot{x}})\delta x dt \tag{2.22}$$

$$\left(\frac{\partial L}{\partial \dot{x}}\delta x\right)_{t_1}^{t_2} = 0 \tag{2.23}$$

Since the boundaries of the function are fixed,

$$\delta x(t)\Big|_{t_1}^{t_2} = 0 \tag{2.24}$$

This yields:

$$\delta A = \int_{t_1}^{t_2}(\frac{\partial L}{\partial x} - \frac{d}{dt}\frac{\partial L}{\partial \dot{x}})\delta x dt \tag{2.25}$$

so the functional derivative is:

$$\frac{\delta A}{\delta x} = \frac{\partial L}{\partial x} - \frac{d}{dt}\frac{\partial L}{\partial \dot{x}} \tag{2.26}$$

So how does this relate to density functional theory?

$$E = \int_V \left(F[n(r)] + v_{ext}(r)n(r)\right)d^3r \tag{2.27}$$

$$\Rightarrow \delta E = \int_V \left(\frac{\partial F}{\partial n} + v_{ext}(r)\right)\delta n d^3r \tag{2.28}$$

The Kohn-Sham equations minimize the energy functional, $E[n(r); v_{ext}(r)]$, with respect to the electron density $n(r)$. The key assumption in the Kohn-Sham equations is for each non-uniform ground-state density $n(r)$ of an interacting electron system, there exists a non-interacting electron system with the same non-uniform ground-state density. This means that the ground-state density of any interacting electron system with N electrons can be decomposed into the sum of N independent orthonormal orbitals, or

$$n(r) = \sum_i \phi_i^*(r)\phi_i(r) \tag{2.29}$$

where i designates the occupied states including the spatial and spin configurations.

Now, it is important to note that this is an exact representation and minimization of the exact ground-state density will provide the exact ground-state energy; however, an approximate process is to minimize equation 2.28. Minimization for this process leads to an optimized (yet approximate) ground-state wavefunction and an approximate upperbound for the ground-state energy. The Coulomb interaction between electrons E_H is also referred to as the Hartree potential defined as:

$$E_H[n] = \frac{1}{2} \int n(r) \frac{e^2}{|r-r'|} n(r') dr dr' \equiv \frac{1}{2} \sum_{ij} \langle \phi_i \phi_j | \frac{e^2}{r_{12}} | \phi_i \phi_j \rangle \equiv \frac{1}{2} \int V_H(r) n(r) d^3r. \quad (2.30)$$

The kinetic energy $T_0[n]$ of the system of non-interacting electrons with the same density is:

$$T_0[n] = \sum_i \langle \phi_i | - \frac{\hbar^2 \nabla^2}{2m} | \phi_i \rangle \quad (2.31)$$

The Hohenberg-Kohn functional can now be written as:

$$E[n(r); v_{ext}] = T_0[n] + E_H[n] + \int v_{ext}(r) n(r) dr + E_{xc}[n] \quad (2.32)$$

where E_{xc} is defined as:

$$E_{xc}[n] = T[n] - T_0[n] + E_{ee}[n] - E_H[n] \quad (2.33)$$

The functional can now be written explicitly as:

$$E[n(r); v_{ext}] = \sum_i \langle \phi_i | - \frac{\hbar^2 \nabla^2}{2m} + v_{ext} | \phi_i \rangle + E_H[n] + E_{xc}[n] \quad (2.34)$$

If we look at the variation $\delta E_{xc}[n]$ using the same notion of the functional derivative that I previously mentioned, it yields:

$$\delta E_{xc}[n] = \int V_{xc}(r) \delta n(r) d^3r = \int V_{xc}(r) \delta \sum_i \phi_i^*(r) \phi_i(r) d^3r \quad (2.35)$$

From the definition of a functional derivative, we know that this means that $V_{xc} \equiv \frac{\delta E_{xc}}{\delta n(r)}$.

Finally, this gives rise to the Kohn-Sham equations that will form the basis of the calculations that were performed in this thesis from first principles. Note the eigenvalue equation that will be performed iteratively until self-consistency:

$$\left[-\frac{\hbar^2 \nabla^2}{2m} + v_{ext}(r) + V_H(r) + V_{xc}(r) \right] \phi_i(r) = \epsilon_i \phi_i(r) \quad (2.36)$$

Please also note that the local density approximation[5] for the exchange-correlation functional is used in my calculations, which is used for slowly varying spatial density $n(r)$. It takes the form:

$$V_{xc}(r) = \frac{\delta E_{xc}[n]}{\delta n(r)} = \epsilon_{xc}(n(r)) + n(r)\frac{d\epsilon_{xc}(n(r))}{dn(r)} \tag{2.37}$$

The simulations in this work were performed using Quantum Espresso[6] with the Projector Augmented Wave[7] formalism. The atomic datasets were generated using ATOMPAW[8] code with a plane wave expansion for the wavefunction and the cut-off radius of $|\mathbf{k+G}|^2 \leq 64$ Ry.

High-performance computing

Data compression is a useful way to manage the vast amount of data that is generated by simulating physical phenomena. One form of compressing data and achieving reduced scaling for large-scale simulations is to factor a large tensor of data into a smaller one and corresponding matrices that will together be an approximation known as the Tucker Decomposition. Although we did not use this technique in our simulations, I explain how to perform this technique[9, 10] and suggest how it can be used in Density Functional Theory simulations in the following way:

The Tucker approximation is when you have a large tensor, a 3-way tensor in this case, and you decompose that tensor into a smaller core tensor and three factor matrices. The core tensor can be any size that is appropriate for the problem that one is trying to solve, but the approximation can be seen in figure 2.1 below: Each entry in the tensor X can be approximated as:

$$x_{ijk} \approx \sum_{p=1}^{P}\sum_{q=1}^{Q}\sum_{r=1}^{R} g_{pqr}\ a_{ip}b_{jq}c_{kr}, \tag{2.38}$$

where x_{ijk} is each entry in X, g_{pqr} is each entry in G, and a_{ip}, b_{jq}, c_{kr} are column vectors in the factor matrices A, B, and C, respectively. The dimensions of X are $I \times J \times K$ which is usually much greater (given how you construct your model) than the dimensions of the tensor G. The dimensions of G are $P \times Q \times R$. One can see that each entry in G is
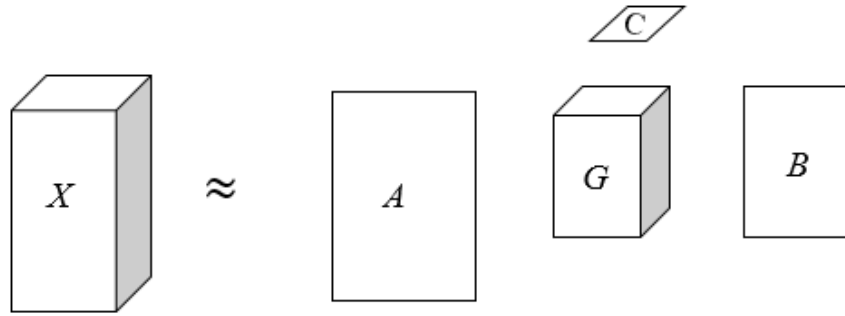
Figure 2.1: Tucker decomposition of a three-way tensor

multiplied by the outer product of each vector in the factor matrices, A, B, and C to give the approximation.

When familiarizing oneself with a data tensor, one must know what modes of a tensor and fibers are in order to understand the algorithm. Modes are the subarrays that form when a subset of the indices are fixed and fibers are the higher-order analogue of matrix rows and columns. A matrix column is a mode-1 fiber and a matrix column is a mode-2 fiber. Third-order tensors have row, column, and tube fibers denoted $x_{:jk}$, $x_{i:k}$, and $x_{ij:}$ respectively in figure 2.2.
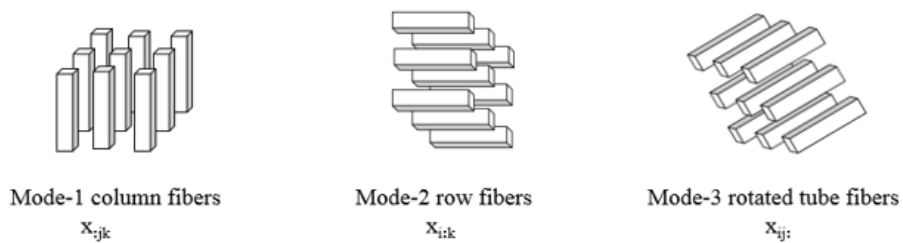
Figure 2.2: Fibers of a third-order tensor

In order to understand what this means when you have data, consider figure 2.3 where there are two matrices, X_1 and X_2. The modes of the tensor are denoted as $X_{(1)}$, $X_{(2)}$, and $X_{(3)}$ for the first, second, and third modes, respectively.

The Sequentially-Truncated Higher-Order Singular Value Decomposition (ST-HOSVD)

$$X_1 = \begin{bmatrix} 1 & 2 & 3 & 4 \\ 5 & 6 & 7 & 8 \\ 9 & 10 & 11 & 12 \end{bmatrix} \qquad X_2 = \begin{bmatrix} 13 & 14 & 15 & 16 \\ 17 & 18 & 19 & 20 \\ 21 & 22 & 23 & 24 \end{bmatrix}$$

The mode-n fibers are:

$$X_{(1)} = \begin{bmatrix} 1 & 2 & 3 & 4 & 13 & 14 & 15 & 16 \\ 5 & 6 & 7 & 8 & 17 & 18 & 19 & 20 \\ 9 & 10 & 11 & 12 & 21 & 22 & 23 & 24 \end{bmatrix}$$

$$X_{(2)} = \begin{bmatrix} 1 & 5 & 9 & 13 & 17 & 21 \\ 2 & 6 & 10 & 14 & 18 & 22 \\ 3 & 7 & 11 & 15 & 19 & 23 \\ 4 & 8 & 12 & 16 & 20 & 24 \end{bmatrix}$$

$$X_{(3)} = \begin{bmatrix} 1 & 5 & 9 & 2 & 6 & 10 & \dots & 4 & 8 & 12 \\ 13 & 17 & 21 & 14 & 18 & 22 & \dots & 16 & 20 & 24 \end{bmatrix}$$

Figure 2.3: Example of modes in a three-way tensor

algorithm[10], which is a parallelized form of the Tucker decomposition can be computed in the following way:

Figure 2.4: Sequentially-Truncated Tucker decomposition of a three-way tensor

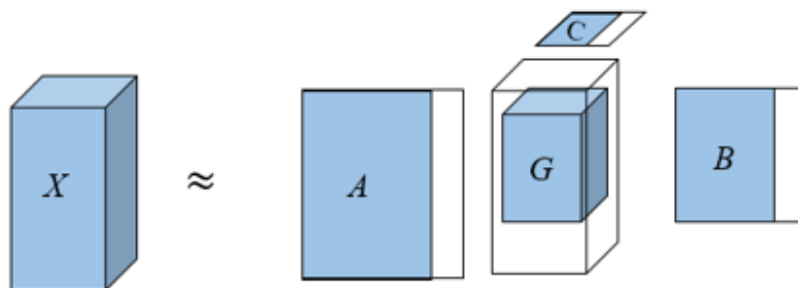1) *procedure* **ST-HOSVD**(X, ϵ)

2) $Y \leftarrow X$

3) *for* $n = 1, \ ..., \ N \ do$

4) $S \leftarrow \ Y_{(n)} Y_{(n)}^T$

5) $R_n \ \leftarrow \ min \ R \ such \ that \ \sum\limits_{r > R} \lambda_r(S) \ \leq \ \dfrac{\epsilon^2 \|X\|^2}{N}$

6) $U_{(n)} \ \leftarrow \ leading \ R \ eigenvectors \ of \ S$

7) $Y \ \leftarrow \ Y \times_n \ U^{(n)T}$

8) *end for*

9) $G \ \leftarrow \ Y$

10) *return* $G, U^{(n)}$

11) *end procedure*

Here, the inputs are the tensor X and machine epsilon. To give an overview, the higher-order SVD decomposition of the first mode is given by:

$$X_{(1)} = U^{(1)} \Sigma^{(1)} V^{(1)T} \tag{2.39}$$

Where $X_{(1)}$ is $I \times JK$, $U^{(1)}$ is $I \times I$, $\Sigma^{(1)}$ is $I \times I$, and $V^{(1)T}$ is $I \times JK$. The algorithm is called truncated because only the first 'P' column vectors of $U^{(1)}$ are selected that satisfy condition (6). Also, one can think of modes of a tensor as "flattening" the tensor to form a matrix.

Now, in order to use this algorithm in DFT, one must figure out how to place equation 2.36 on a grid in such a way that will contain the correct physics in the reduced Tucker basis. Ay, there is the rub.

In addition to the Tucker Decomposition, another effective way to cut convergence times for matrix multiplication is to use Strassen's algorithm[11]. We did not use this algorithm in our simulations, but I believe that one would find it useful. Matrix multiplication is the most time consuming aspect of scientific computing because it scales as $O(n^3)$, where n is usually the number of atoms in your system, and Strassen's algorithm effectively reduces eight matrix multiplications in a square matrix–when the size of the matrix is sufficient enough to overcome the increased number of matrix additions and subtractions (meaning

at least 16×16 square matrices), because the number of arithmetic operations approximately scale as $O(n^{2.81})$. This difference in the exponent makes a significant difference when one's system is large. Although I am not certain how Strassen formulated his algorithm, one can think of a simpler case when considering how his algorithm works. For instance, consider the multiplication $(a + bi)(c + di)$ where a, b, c, and d are positive constants. Normally, this multiplication would take take a total of four multiplications when using the FOIL method to produce $(ac - bd) + (ad + bc)i$. There is a way, however, to do the above multiplication in three steps, and that is to multiply $(a + b)(c - d)$ [I] (meaning do the addition and substraction first), ad [II], and bc [III]. To get the total product, one would need to take $(I + II - III) + (II + III)i$ to get $(ac - bd) + (ad + bc)i$.

In a similar way, Stassen takes the multiplication of two square matrices A and B, where $A = \begin{pmatrix} A_{11} & A_{12} \\ A_{21} & A_{22} \end{pmatrix}$ and $B = \begin{pmatrix} B_{11} & B_{12} \\ B_{21} & B_{22} \end{pmatrix}$, and multiplies them in such a way that there are seven matrix multiplications (which is significant because matrix multiplication is more expensive than matrix addition or subtraction between matrices). If one wants to analyze the difference between Strassen's algorithm and normally multiplying two 2×2 matrices, one must consider the following:

$$C = AB = \begin{pmatrix} C_{11} & C_{12} \\ C_{21} & C_{22} \end{pmatrix}$$

Normal:

$C_{11} = A_{11}B_{11} + A_{12}B_{21}$

$C_{12} = A_{11}B_{12} + A_{12}B_{22}$

$C_{21} = A_{21}B_{11} + A_{22}B_{21}$

$C_{22} = A_{21}B_{12} + A_{22}B_{22}$

Strassen (note that the additions and subtractions in the parenthesis should be

performed first like the example above):

$I = (A_{11} + A_{22})(B_{11} + B_{22})$

$II = (A_{21} + A_{22})B_{11}$

$III = A_{11}(B_{12} - B_{22})$

$IV = A_{22}(-B_{11} + B_{21})$

$V = (A_{11} + A_{12})B_{22}$

$VI = (-A_{11} + A_{21})(B_{11} + B_{12})$

$VII = (A_{12} - A_{22})(B_{21} + B_{22})$

$C_{11} = I + IV - V + VII$

$C_{21} = II + IV$

$C_{12} = III + V$

$C_{22} = I + III - II + VI$

Please note that Strassen's algorithm can be written in such a way that exploits how the matrices are stored in the cache (i.e. column-major, zig-zag, etc.) in order to minimize the amount of cache-misses and to get even higher performance[12, 13].

Chapter 3

$Na_4P_2S_6$

In 1982, Mercier et al.[14] analyzed the structure for $Li_4P_2S_6$ and concluded that the structure was the hexagonal space group, $P6_3/mcm$; however, in 2014, Kuhn et al.[15] concluded that the structure for $Na_4P_2S_6$ was the monoclinic space group, $C2/m$. This presents a structural puzzle because the only difference between the two compounds is the cation, and it produces the question, why does exchanging lithium ions for sodium ions in the same compound produce a different arrangement of atoms? Also, how does this affect the electronic properties of the material? The goal of my research is to find materials that can be suitable solid-state electrolytes for sodium-ion batteries, and this structural puzzle could shed light on the difference between sodim-ion electrolytes and lithium-ion electrolytes. It could also provide information on how to improve the conductivity of sodium-ion electrolytes, especially if one wants to use them to replace their lithium-ion analogues in battery techonology in some instances. The monoclinic space group, $C2/m$, which can be seen in figures 3.1 and 3.2, has very low symmetry compared to the hexagonal space group, $P6_3/mcm$, because there are only four symmetry elements compared to twenty-four, so one expects that these different geometries might have remarkable differences in formation energies and differences in conductivity.

It is important to note that for this paper, I did all of the calculations for $Na_4P_2S_6$ (except for the partial density of states plots) while Dr. Natalie Holzwarth did all of the calculations for $Li_4P_2S_6$. A subgroup of the Mercier structure, space group $P\bar{3}1m$ which is based on a hexagonal bravais lattice shown in figure 3.3 and figure 3.4, was studied in place of the Mercier structure because of the difficulty when modeling such a disordered structure
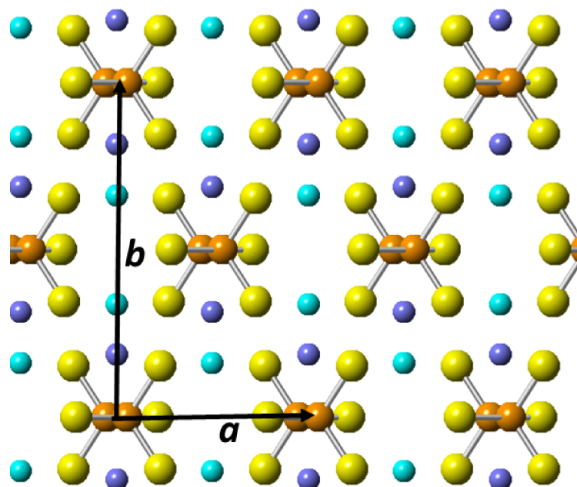
Figure 3.1: Ball-and-stick model of C2/m in the ab-plane. The Na, P, and S sites are represented by the blue, orange, and yellow balls, respectively. There are two different sodium sites (denoted 'g' and 'h' sites in the Wyckoff label) for space group C2/m, which is represented by two shades of blue balls.

Figure 3.2: Ball-and-stick model of C2/m in the bc-plane with the same convention as figure 3.1.

with a periodically repeating framework that forms the basis of our simulations (i.e. the Projector Augmented Wave (or PAW) method[7]). The Na, P, and S sites are represented by the blue, orange, and yellow balls, respectively. There are two different sodium sites (denoted 'c' and 'd' sites in the Wyckoff label) for space group P$\bar{3}$1m, which is represented
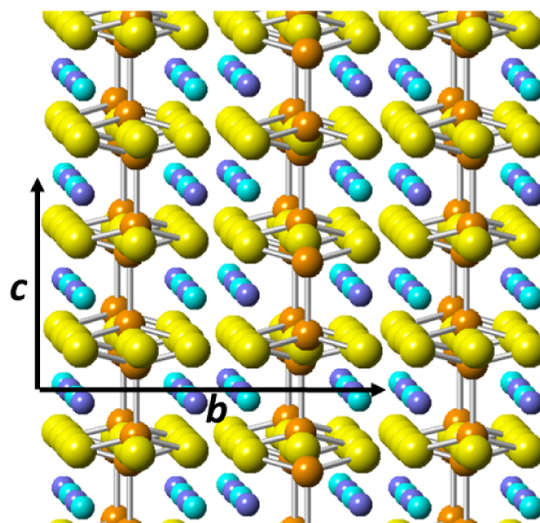
by two shades of blue balls represented in figures 3.3 and 3.4.
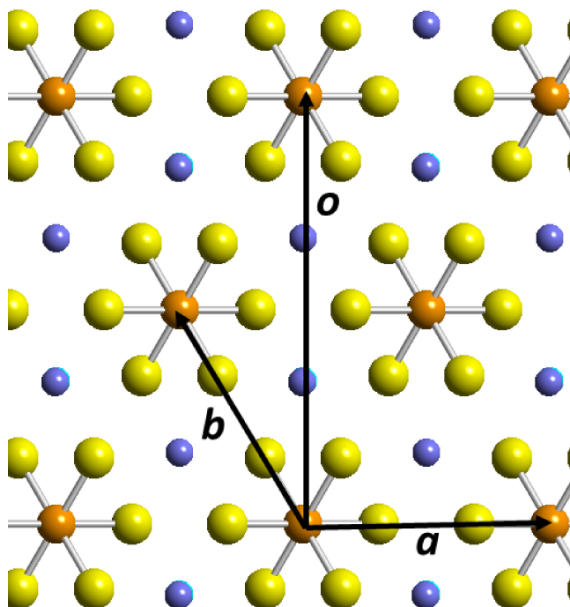
Figure 3.3: Ball-and-stick model of P$\bar{3}$1m showing a projection onto the hexagonal plane
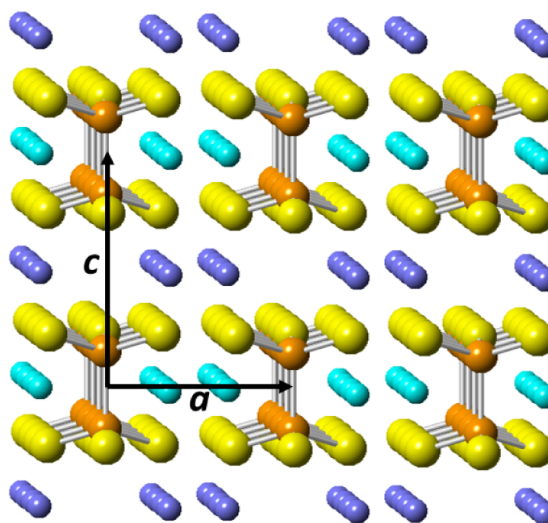
Figure 3.4: Ball-and-stick model of P$\bar{3}$1m showing a view that includes the c axis.

The disordered ground states for P6$_3$/mcm, space groups Pnnm and Pnma that can be seen in figures 3.5 and 3.6, respectively, were used for both Li$_4$P$_2$S$_6$ and Na$_4$P$_2$S$_6$ because they were derived from analyzing the disorder structures of Li$_4$P$_2$S$_6$ in terms of

the placements of the P_2S_6 units along the hexagonal c-axis in a previous study by Hood et al[16].

Figure 3.5: Ball-and-stick model of Pnnm using the same convention in figure 3.3

Figure 3.6: Ball-and-stick model of Pnma

In order to understand the geometric relationship between the space groups P$\bar{3}$1m,

Pnnm, Pnma, and C2/m, consider the following:

$$\vec{a}_{Kuhn} = \vec{a}_{hex}, \ \vec{b}_{Kuhn} = \vec{o}_{hex}, \ and \ \vec{c}_{Kuhn} = \vec{c}_{hex}, \quad (3.1)$$

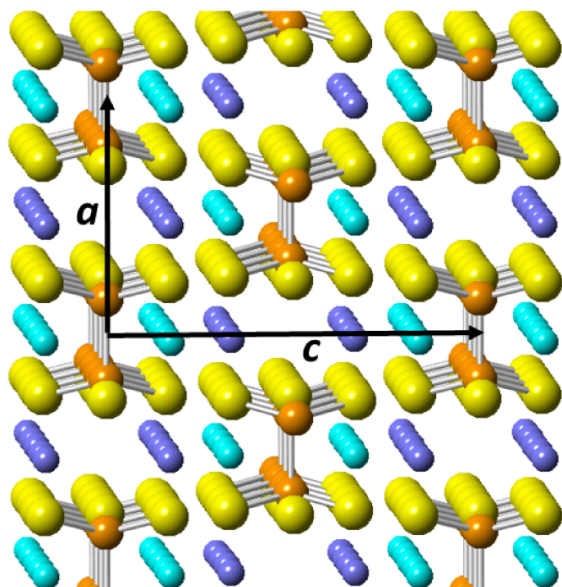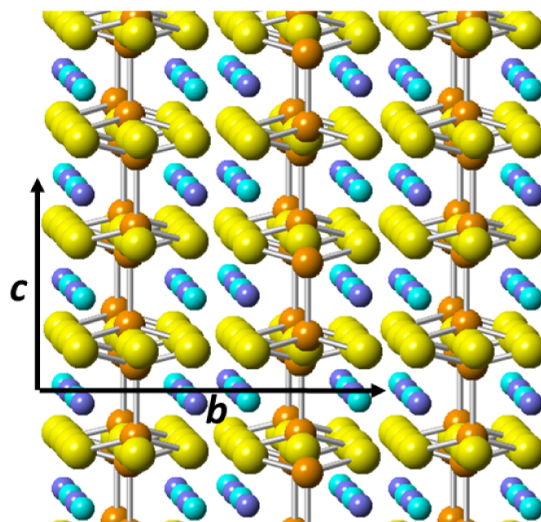where $\vec{a}_{Kunh}$, $\vec{b}_{Kunh}$, $\vec{c}_{Kunh}$ are the lattice vectors in C2/m, and $\vec{a}_{hex}$, $\vec{o}_{hex}$, $\vec{c}_{hex}$ are the hexagonal vectors defined in figure 3.3.

When considering figure 3.5, the geometric relationship is:

$$\vec{a}_{Pnnm} = \vec{c}_{hex}, \ \vec{b}_{Pnnm} = \vec{a}_{hex}, \ and \ \vec{c}_{Pnnm} = \vec{o}_{hex}, \quad (3.2)$$

where $\vec{a}_{Pnnm}$, $\vec{b}_{Pnnm}$, and $\vec{c}_{Pnnm}$ are the lattice vectors in Pnnm.

Lastly, when considering figure 3.6, the geometric relationship is:

$$\vec{a}_{Pnma} = 2\vec{a}_{hex}, \ \vec{b}_{Pnma} = \vec{o}_{hex}, \ and \ \vec{c}_{Pnnm} = \vec{c}_{hex}, \quad (3.3)$$

where $\vec{a}_{Pnma}$, $\vec{b}_{Pnma}$, and $\vec{c}_{Pnma}$ are the lattice vectors in Pnma.

To begin to compare the conductive properties of the two compounds and the different arrangements for them (meaning space groups C2/m, P$\bar{3}$1m, and Pnma), I constructed vacancies for those geometries in order to run Nudged Elastic Band (NEB)[20, 21, 22] calculations and obtain conductivities for them. The migration path for P$\bar{3}$1m can be seen in figure 3.7, and the corresponding migration energy from the NEB calculations is in figure 3.8. The migration path for C2/m can be seen in figure 3.9, and the corresponding migration energy from the NEB calculations is in figure 3.10. The migration path for Pnma can be seen in figure 3.11, and the corresponding migration energy from the NEB calculations is in figure 3.12.

The results indicated that the migration energy for Pnma structure of $Na_4P_2S_6$ was lower than $Li_4P_2S_6$ along the a-axis (or migration between "d" atoms according to the Wyckoff label), and the migration was higher and lower in certain directions for the P$\bar{3}$1m and C2/m structures. When migrating from one type of ion to the next, meaning going from "c" to "d" in P$\bar{3}$1m and "g" to "h" in the C2/m structure, sodium ions have a slightly higher migration energy than its lithium-ion counterpart. Migration energies for ion migration in between the P_2S_6 were lower for sodium with respect to its lithium

Figure 3.7: Ball-and-stick model of migration path for P$\bar{3}$1m
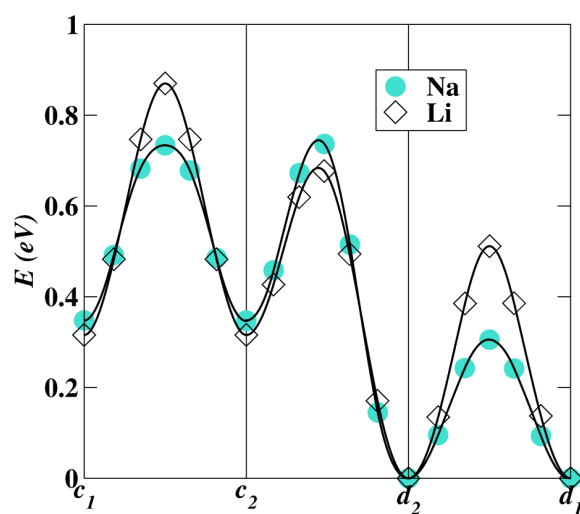
Figure 3.8: Activation energy for the migration path in figure 3.7 for $Na_4P_2S_6$ and $Li_4P_2S_6$

Figure 3.9: Ball-and-stick model of migration path for C2/m
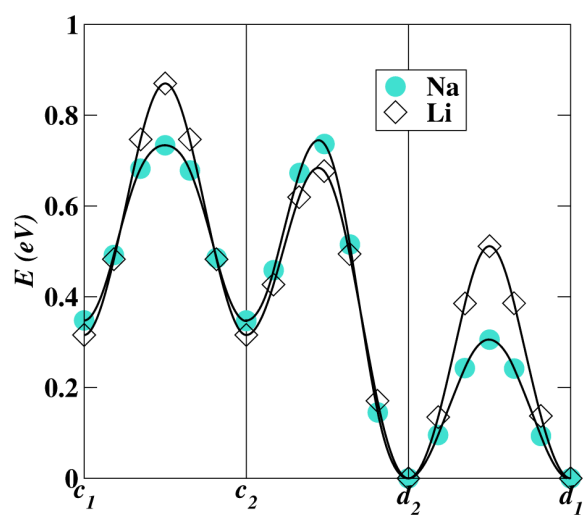
Figure 3.10: Activation energy for the migration path in figure 3.9 for $Na_4P_2S_6$ and $Li_4P_2S_6$
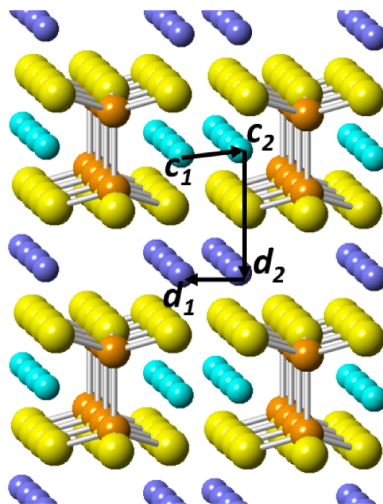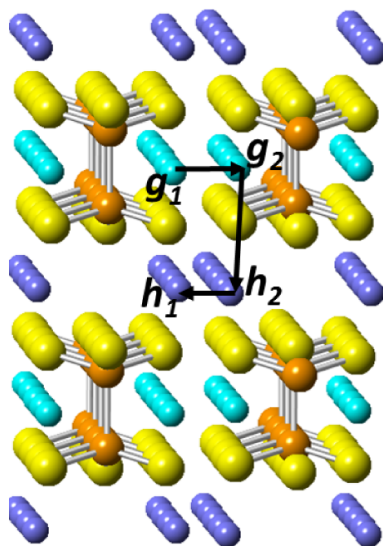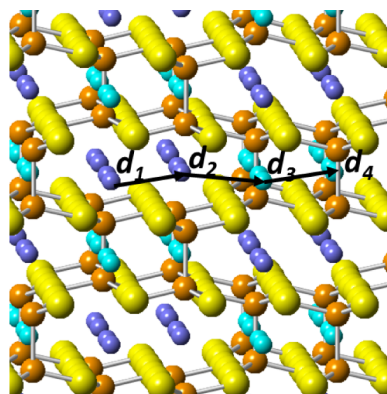
Figure 3.11: Ball-and-stick model of migration path for Pnma
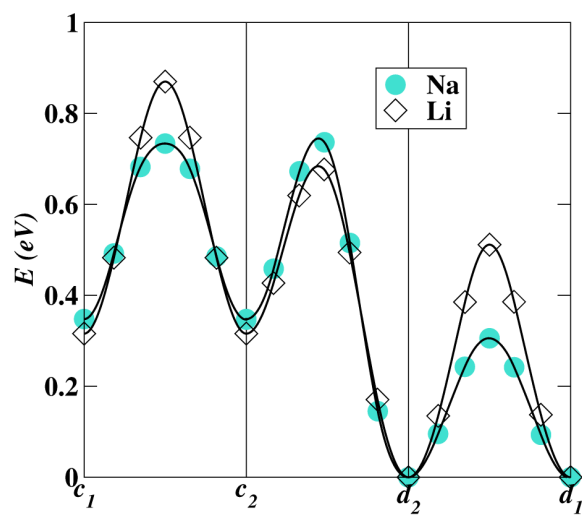
Figure 3.12: Activation energy for the migration path in figure 3.11 for $Na_4P_2S_6$ and $Li_4P_2S_6$

Space group	Site	$Na_4P_2S_6$	$Li_4P_2S_6$
$C2/m$; No. 12	Na/Li g	0.40	0.52
	Na/Li h	0.00	0.00
$P\bar{3}1m$; No. 162	Na/Li c	0.35	0.32
	Na/Li d	0.00	0.00
$Pnma$; No. 62	Na/Li d	0.15	0.11
	Na/Li d	0.00	0.00

Figure 3.13: Vacancy energy (in eV) for the migration paths for $Na_4P_2S_6$ and $Li_4P_2S_6$

$Na_4P_2S_6$	$Na_4P_2S_6$	$Li_4P_2S_6$
$C2/m$	-11.47	-12.07
$P\bar{3}1m$	-11.47	-12.42
$Pnnm$	-11.56	-12.46
$Pnma$	-11.56	-12.46

Figure 3.14: Heats of formation (in eV per formula unit) for the four optimized structures in $Na_4P_2S_6$ and $Li_4P_2S_6$

counterpart in both $P\bar{3}1m$ amd $C2/m$ structures, but migration energies for ion migration above and below those units were lower for lithium with respect to its sodium counterpart. A comparison of the activation energy for the structures between $Na_4P_2S_6$ and $Li_4P_2S_6$ can be seen in figure 3.13.

The heats of formation is another important measure when ascertaining the difference between the various geometries for $Na_4P_2S_6$ and $Li_4P_2S_6$, because the structure with the lowest amount of energy (or enthalpy) it takes to form the compound will be the most likely structure to form in nature. After analyzing the enthalpy for each structure per formula unit of $Na_4P_2S_6$ and $Li_4P_2S_6$, the most probable geometries for both $Na_4P_2S_6$ and $Li_4P_2S_6$ are Pnnm and Pnma. These are the models for the Mercier structure (or the disordered structure models), and the difference in energy between these structures and the others for $Na_4P_2S_6$ was 0.09 eV per formula unit. The results can be seen in figure 3.14. These calculations suggest that the Kuhn structure is meta-stable.

Chapter 4

Na$_3$SbS$_4$

As part of an effort to develop energy storage technology based on all-solid-state Na-ion batteries, recent papers in the literature[17, 18, 19] demonstrate the electrochemical stability of the solid electrolyte Na$_3$SbS$_4$ interfaced with a metallic Na anode. The integrity of this electrolyte/anode interface, which is essential to the success of these battery components, is attributed to the formation of a stable solid-electrolyte interphase (SSEI). We report the results of a computational study of this system, using first principles methods to model ideal interfaces of Na$_3$SbS$_4$ with Na metal. The ideal interfaces were constructed from (110), (100), and (001) surfaces of tetragonal crystals of Na$_3$SbS$_4$ and Na metal in various configurations. The results show several likely components of the SSEI including a few broken SbS bonds and Na$_2$S groups stabilized at the outer layer of the interface.

Before we investigated the Na$_3$SbS$_4$/Na interface, we constructed the (100), (001), and (110) surfaces for Na$_3$SbS$_4$ with the intention of calculating the surface with the lowest energy. The lowest energy surface would be presumed to be the most probable surface that forms when creating a solid-state battery, and the intensive parameter, γ, was used to calculate the most probable surface. The surface energy γ is defined as,

$$\gamma = \frac{E_{total} - n_{bulk}E_{bulk}}{2A},$$
(4.1)

E_{total} is the total energy of the supercell for the simulation that contains n_{bulk} unit cells. E_{bulk} is the energy of a single unit cell for Na$_3$SbS$_4$ and $2A$ is the total cross-sectional area for the interface.

As reported in Wang et al.[17], there are two phases for Na$_3$SbS$_4$: a low temperature phase, and a high temperature phase. We modeled the low temperature phase by

creating a supercell of the figure below to create the (100), (001), and (110) surfaces.The low temperature phase, space group $P\bar{4}2_1c$, has two distinct sodium sites labelled "a" and "d" in the Wyckoff label and is tetragonal, thus the material has two different lattice constants labelled "a" and "c" in figure 4.1.

Low temperature phase Na$_3$SbS$_4$ (space group $P\,\bar{4}\,2_1\,c$)

1 x, y, z	5 $\frac{1}{2}+x, \frac{1}{2}-y, \frac{1}{2}-z$
2 $\bar{x}, \bar{y}, z$	6 $\frac{1}{2}-x, \frac{1}{2}+y, \frac{1}{2}-z$
3 $y, \bar{x}, \bar{z}$	7 $\frac{1}{2}+y, \frac{1}{2}+x, \frac{1}{2}+z$
4 $\bar{y}, x, \bar{z}$	8 $\frac{1}{2}-y, \frac{1}{2}-x, \frac{1}{2}+z$

2b 8e 2a 4d   Wyckoff labels

Sb S Na Na   Atoms
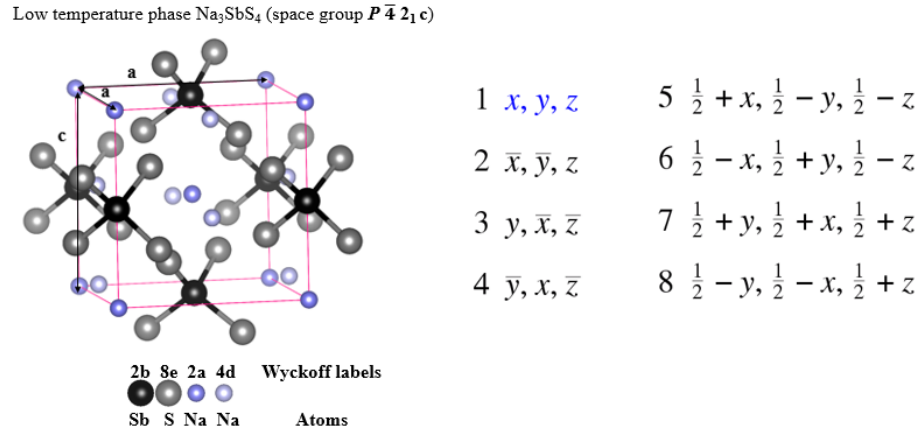
Figure 4.1: Ball-and-stick model of low temperature Na$_3$SbS$_4$ with corresponding symmetry elements

Sb S Na
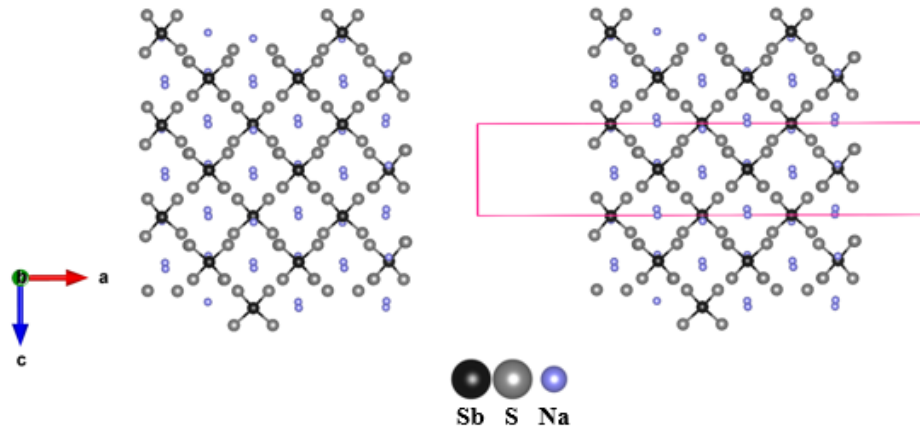
Figure 4.2: Ball-and-stick model of (100) surface with vacuum

The (100) surface was constructed by creating a supercell, or more specifically, 5 unit cells of Na$_3$SbS$_4$ and removing atoms along the "a-axis" until the vacuum was approximately 15 Å thick. Figure 4.2 illustrates how the (100) surface was constructed. The (100) surface normal is along the a-axis, and the pink rectangle represents the supercell of

5 unit cells of Na_3SbS_4 that was constructed. As one can see, atoms were removed within the rectangle so that the (100) surface could be constructed. The image on the left is a periodically repeated image of the right. One can think of there being an infinite amount of periodically repeating images, but I just illustrated two of them to show the width in between the surfaces.
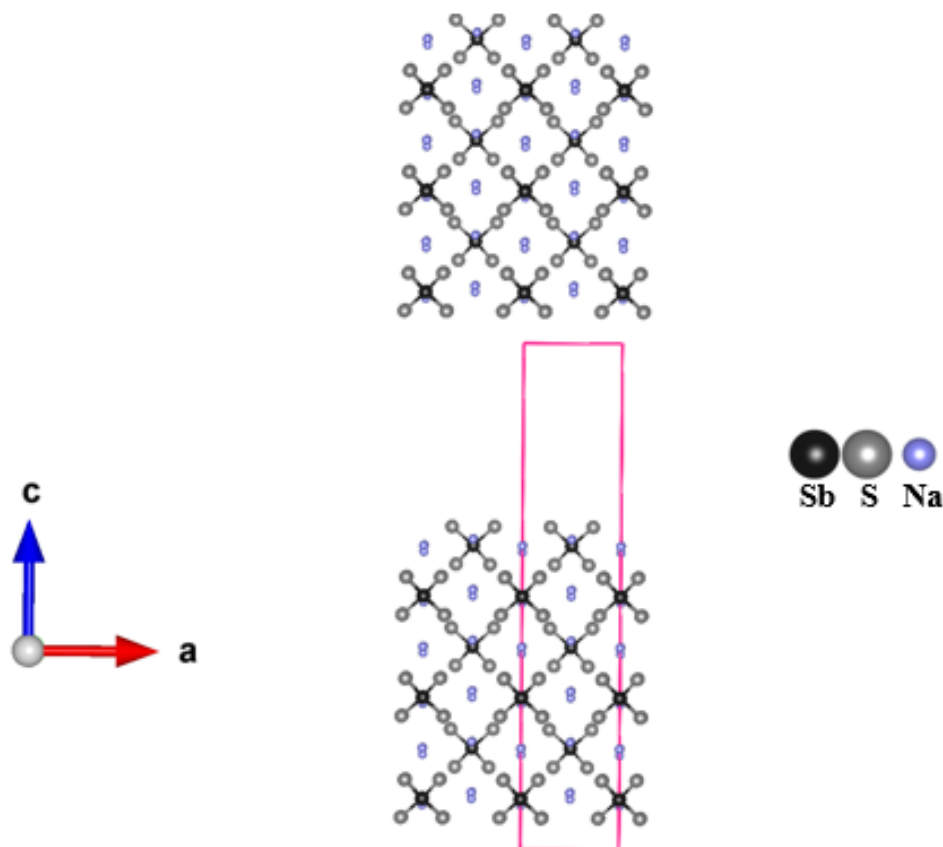
Figure 4.3: Ball-and-stick model of (001) surface with vacuum

Similarly, the (001) suraface was constructed by generating a 5 times larger unit cell along the c-axis and removing atoms within the rectangle until a vacuum thickness of approximately 15 Å . Figure 4.3 illustrates how the (001) surface was constructed. The material on the top is just a periodically repeated image of what is on the bottom. Again, I showed two images to illustrate the width of the surface.

Lastly, I constructed the (110) surface by creating a supercell of the surface that is along the diagonal of the cube from edge to edge through the center, meaning, if a sharp

plane (i.e. a knife) were to cut the square base of Figure 4.1 along this surface, it would split the rectangular prism into two triangular prisms. I then rotated the crystallographic coordinate system such that the surface normal pointed in the vertical direction. Figure 4.4 illustrates how the (110) surface was constructed. It is important to note that the "a'" and
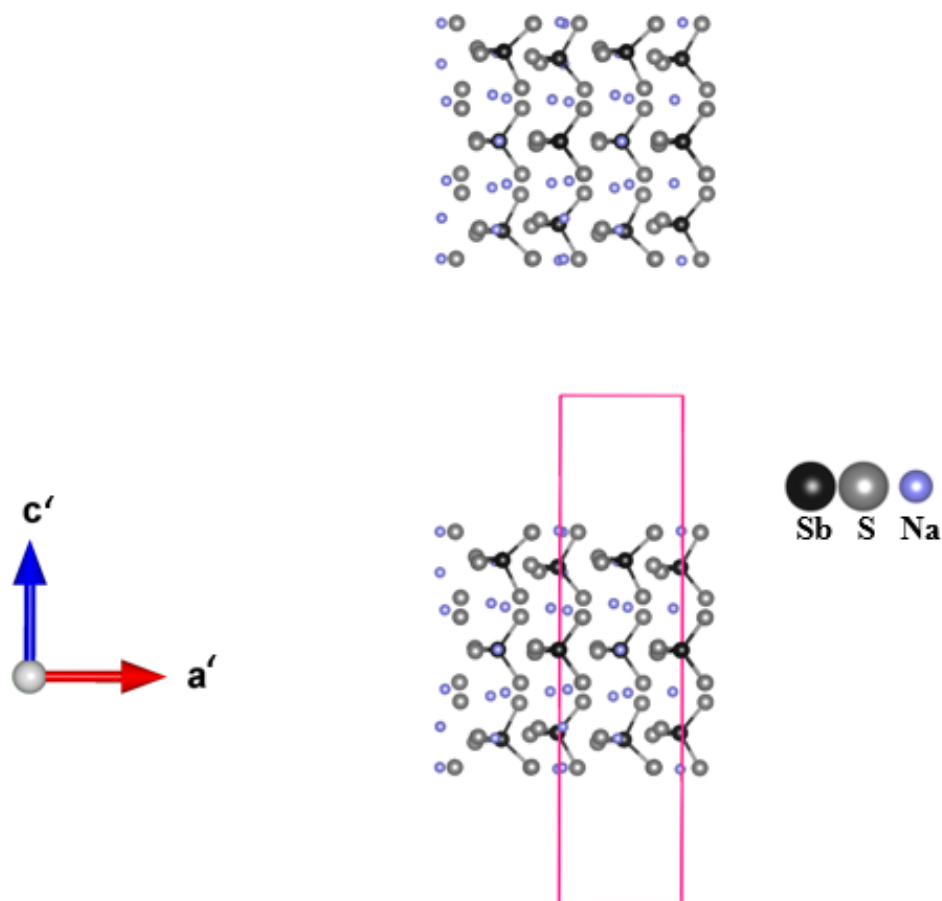
Figure 4.4: Ball-and-stick model of (110) surface with vacuum

"c'" directions are different from the "a" and "c" directions in the (001) and (100) surfaces because the coordinate frame has been rotated. "a'" $= \vec{c}$, "c'" $= \sqrt{\frac{1}{2}} \left(\vec{a} + \vec{b} \right)$, and "b'" $= \sqrt{\frac{1}{2}} \left(\vec{a} - \vec{b} \right)$. This surface was constructed by enlarging the cell to be 5 times as large as the normal unit cell for the (110) direction, and atoms were removed until there was a vacuum thickness of approximately 15 Å . It is also important to note that in order to construct this surface, two sodium atoms must be removed from the top and bottom of the surface in order to have the correct ratio of atoms in Na_3SbS_4. I tested 12 different permutations (or two

times four-choose-two) of the possible configurations, and Figure 4.4 is the configuration with the lowest energy (thus presumed to be the most probable structure).

One might ask the question, how did I choose the seemingly arbitrary size of three layers for the (100), (001), and (110) Na_3SbS_4 surfaces (which are six, six, and twelve formula units, respectively, since the (110) surface takes twice as many formula units to construct as the (001) and (100) surfaces)? To answer that, I calculated the intrinsic parameter, γ, for up to 8 formula units for the (001) surface with a six formula unit comparison to the (100) surface and an addition test of higher and lower vacuum thickness for the six formula unit (001) surface, which can be seen in Figure 4.5 below.
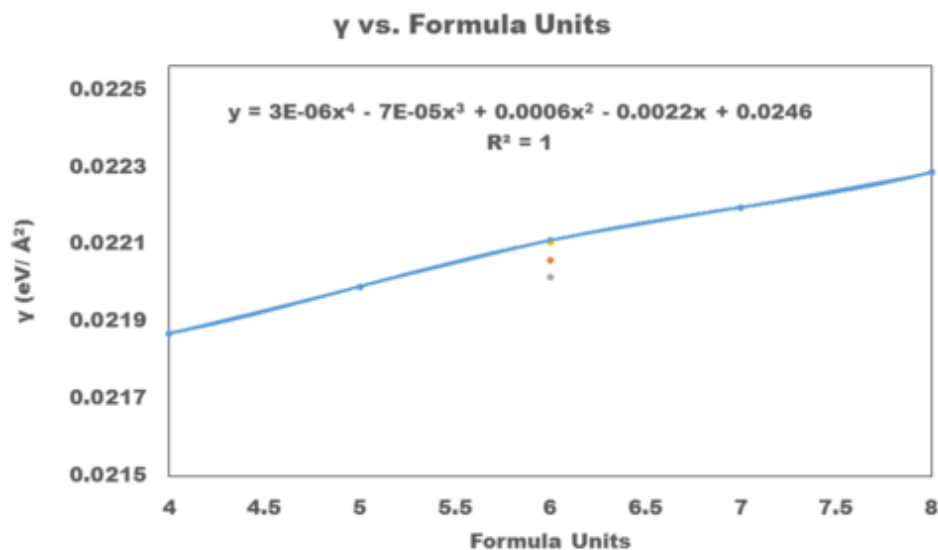

γ vs. Formula Units

$y = 3E\text{-}06x^4 - 7E\text{-}05x^3 + 0.0006x^2 - 0.0022x + 0.0246$

$R^2 = 1$

Figure 4.5: Plot of γ (eV/$\mathring{A}^2$), or the amount of energy it takes to create a surface per surface area of the interface, for the (001) and (100) surfaces. The blue line is for the (001) surface and the gray dot is the six formula unit (100) surface

The blue dots represent γ for six formula units of the (001) surface with approximately $15\mathring{A}$ for the thickness of the vacuum layer, the gray dot corresponds to γ for six formula units of the (001) surface with approximately $22\mathring{A}$ for the thickness of the vacuum layer, the yellow dot corresponds to shrinking the thickness of the vacuum layer for the (001) surface to approximately $10\mathring{A}$, and the purple dot corresponds to γ for six formula units of the (100) surface with approximately $15\mathring{A}$ for the thickness of the vacuum layer. One can see that altering the vacuum and switching surfaces between the (001) and (100) surfaces when the layer thickness of the vacuum is constant adds approximately 1 meV/$\mathring{A}^2$

for γ, which is within the noise or error of the calculation itself, so one can safely assume that arbitrarily choosing the layer thickness for the vacuum size and the amount of layers of Na_3SbS_4 that one will use for the interface for the sake of convenience when factoring in convergence times is a relatively inconsequential assumption based on this data. Therefore, we choose to model the interface of Na_3SbS_4/Na using three layers of Na_3SbS_4. The question now becomes, how does the (110) surface compare with these two surfaces when calculating the amount of energy it takes to create the surface per area of the interface of the surface, or γ? To answer this, I calculated γ for all possible configurations of the (110) surface for Na_3SbS_4. The figure below shows how γ changes when considering the different configurations of removing two sodium atoms from the top of the surface and the bottom of the surface to achieve the right ratio of Na:Sb:S atoms in Na_3SbS_4.
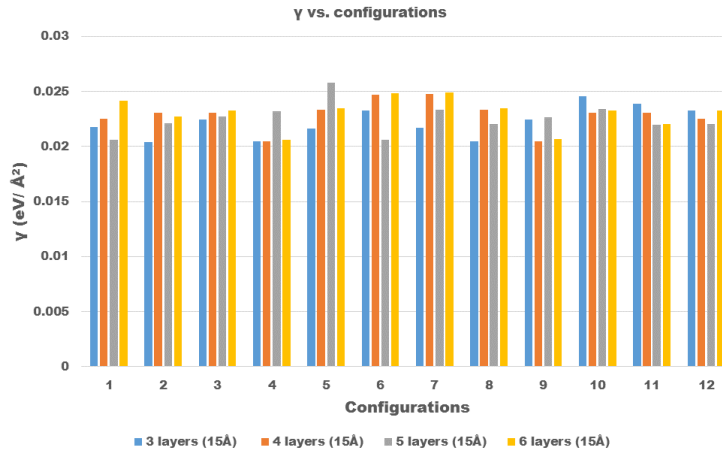

Figure 4.6: Plot of γ $(eV/\mathring{A}^2)$, or the amount of energy it takes to create a surface per surface area of the interface, for the (110) surface with all configurations

Figure 4.6 shows that the minimum energy to create the surface per unit area of the interface was 20 $meV/\mathring{A}^2$, which is approximely 1-2 $meV/\mathring{A}^2$ lower than the (001) and (100) surface with 3 layers of Na_3SbS_4. That difference is within the error of Density Functional Theory calculations, so we decided to perform interfacial simulations with all surfaces because they are all equally probable.

To further test whether or not the selection to represent Na_3SbS_4 with three layers for the interface with metallic Na, I calculated the parameter, $\Delta d/d$, which will tell how

much selected atoms within certain layers move after creating the surface and allowing the atoms to "relax" in Quantum Espresso with respect to the distance before relaxing the atoms, meaning all of the atoms in the system were allowed to move freely to find a minimum in energy where they prefer to sit. The following figure shows how much the atoms moved to indicate whether or not the surface would be stable enough to perform calculations with the interface with metallic sodium:
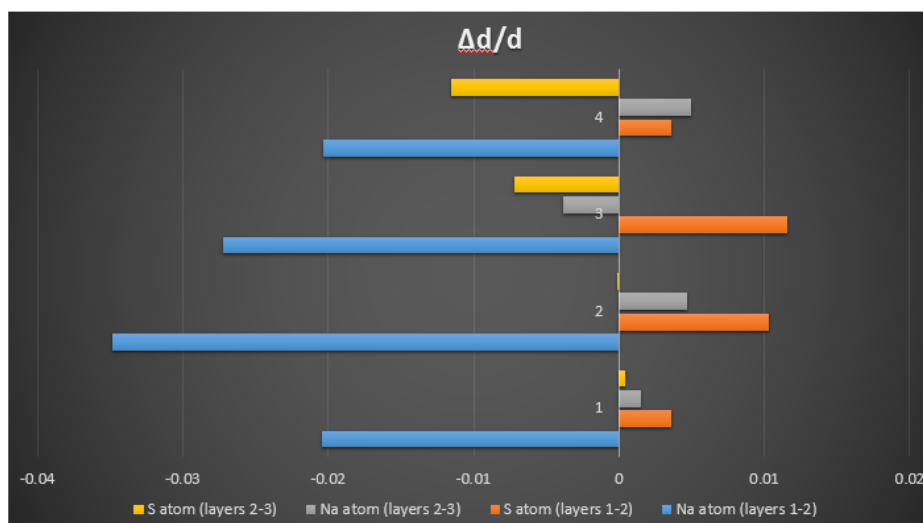

Figure 4.7: Plot of Δd/d, or the amount that selected atoms moved after running "relax" in Quantum Espresso for the entire surface. Δd is the change in distance between layers after relaxation and d is the distance between the layers before relaxation

The negative values in Figure 4.7 correspond to the selected atoms moving inward (meaning away from the vacuum layer) and the positive values correspond to those atoms moving toward the vacuum layer. The atoms that were selected were the same sodium or sulfur atoms for the (001), (100), or (110) surfaces, and they were selected from the first layer closest to the vacuum layer to the second and the third. Since there were two formula units per layer for the (001) and (100) surface (and double for the (110) surface), the third layer of sodium or sulfur corresponded to the center of the surface. The numbers in Figure 4.7 have the following corresponding meanings:

```
1 = 3 layers (or 6 formula units) of (001) Na3SbS4 with 15 vacuum
2 = 3 layers (or 6 formula units) of (100) Na3SbS4 with 15 vacuum
3 = 3 layers (or 12 formula units) of (110) Na3SbS4 with 15 vacuum
4 = 3 layers (or 6 formula units) of (001) Na3SbS4 with 22 vacuum
```

As you can see, atoms minimally move when allowed to find spaces within the material that give a minimum energy for the surface, so establishing that each surface will be three layers thick for Na_3SbS_4 in the interface with sodium is seemingly practical based on the tests that were performed.

Finally, as a last measure of whether or not we could model the surfaces of Na_3SbS_4 using a smaller thickness, I performed Density of States (DOS) plots for the surface of Na_3SbS_4 vs the bulk interior. Figures 4.8 and 4.9 show the charge distribution on each atom in the DOS for Na_3SbS_4 at the surface and in the bulk interior for 4 formula units and 5 formula units of the (001) surface, respectively. The top DOS plots for figures 4.8 and 4.9 are the atoms in Na_3SbS_4 at the surface and the lower DOS plots are the atoms in the bulk (or in between the top and bottom of the surface). I chose 4 and 5 formula units to test because it would speed up convergence times, but the fact that the top and bottom DOS plots don't match means that 6 formula units is a good lower limit.
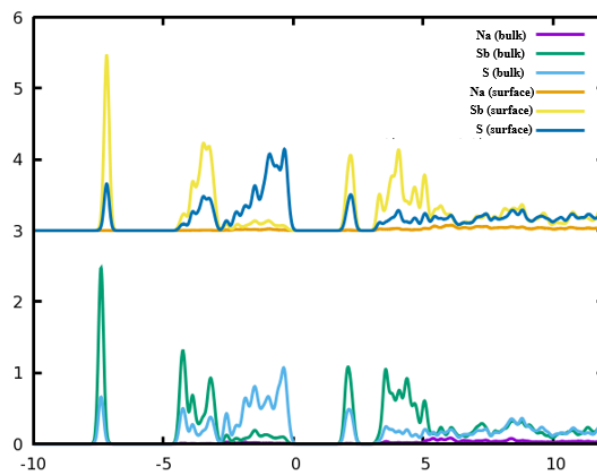

Figure 4.8: DOS plots for 4 formula units of (001) Na_3SbS_4

Now that the problem of how to represent the surfaces of Na_3SbS_4 for the interface has been decided, I then began the next phase of modelling the anode and the electrolyte by stacking metallic sodium on top of the surface of Na_3SbS_4.

Figure 4.10 represents the model of the (110) Na_3SbS_4/Na interface that was created by stacking blocks of sodium on top of the solid-state electrolyte. Since the blocks of sodium on top of Na_3SbS_4 could have led to strain (due to the lack of the cubic materials not being commensurate with one another), the system was allowed to expand or contract along

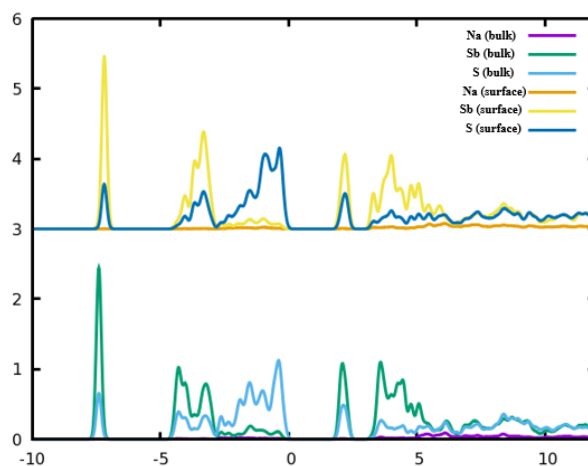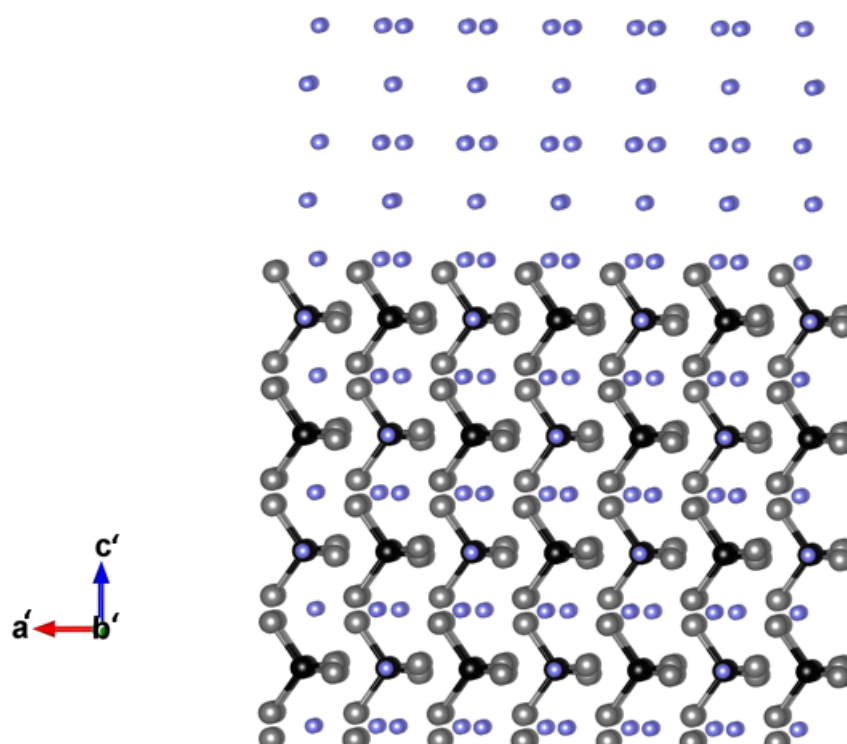Figure 4.9: DOS plots for 5 formula units of (001) Na$_3$SbS$_4$

Figure 4.10: Ball-and-stick model of the initial (110) surface for Na$_3$SbS$_4$

the direction of the surface normal. That is to say, the system was under the conditions of "vc-relax" where the degrees of freedom were restricted to one degree, which was the vertical direction or the direction that is perpendicular to the surface of (110) Na$_3$SbS$_4$.
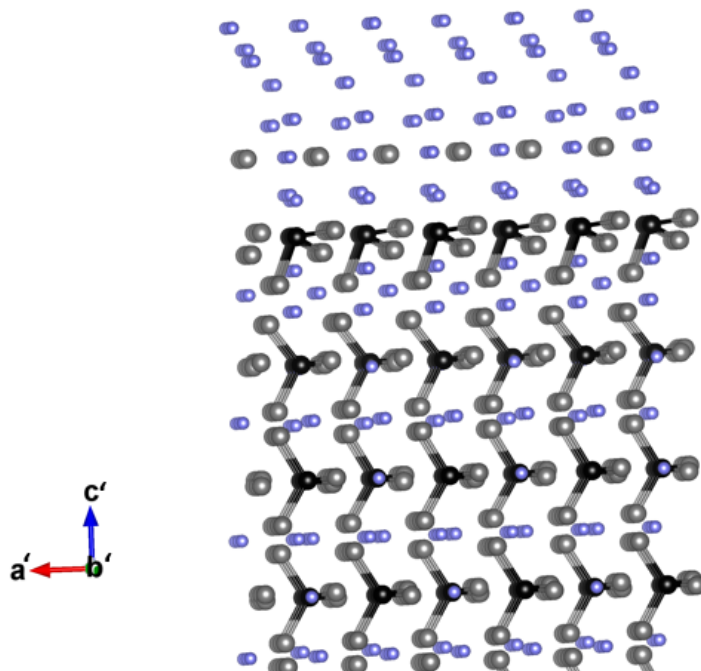
Figure 4.11: Ball-and-stick model of the vc-relaxed (110) surface for Na_3SbS_4

Figure 4.11 indicates that Na_3SbS_4 decomposes at the interface with metallic sodium, and based on how sulfur moves from the bulk structure and surrounds itself with proportionate amounts of metallic sodium (almost like escaping into the sea of sodium), it suggests that Na_2S is forming, which leaves Na_3SbS_3 at the surface. This would suggest that Sb undergoes a change in oxidation state, from a +5 state to a +3 state, when the electrolyte comes in contact with the anode at the interface. We believe that these components of the interface (both Na_3SbS_3 and Na_2S) contribute to what is known as the stable solid-electrolyte interphase layer (or SSEI layer), which can lead to a gradual loss of capacity of a battery if the thickness of the SEI layer grows too large. In order to confirm that Na_3SbS_3 and Na_2S form at the interface between metallic Na and Na_3SbS_4, I decided to plot the DOS of the bulk materials and compare it to the bulk and surface atoms of the simulation from Figure 4.12. The following figure illustrates this comparison:

As one can see from Figure 4.12, the (110) Na_3SbS_4/Na interface DOS is in fairly good agreement with the DOS of the bulk materials, so this further confirms that Na_3SbS_3 and Na_2S form at the interface. This was only for one surface of Na_3SbS_4 and for one configuration of stacking sodium, so further testing is needed to confirm this basis.
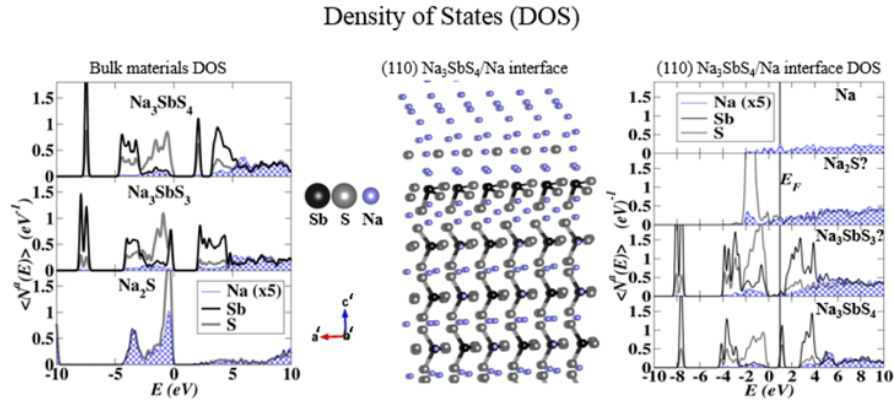
Density of States (DOS)

Figure 4.12: Ball-and-stick model of the vc-relaxed (110) surface for Na$_3$SbS$_4$ and the corresponding DOS for each layer, along with the DOS of the bulk materials: Na$_3$SbS$_4$, Na$_3$SbS$_3$, and Na$_2$S

Another way to represent the Na$_3$SbS$_4$/Na interface was to stack sodium on top of the (100) Na$_3$SbS$_4$ surface and allow the system to expand or contract along the direction of the surface normal, or to state it another way, to run "vc-relax" in Quantum Espresso and allow the degree of freedom to be along the a-axis for the (100) surface. Figure 4.13 illustrates this interface.
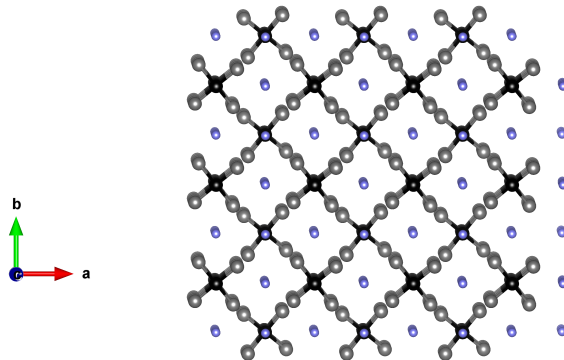

Figure 4.13: Ball-and-stick model of the (100) surface for Na$_3$SbS$_4$ with metallic sodium stacked on top along the a-axis

It is important to note that this model periodically repeats and there is no vacuum between the periodically repeating interfacial images, rather only sodium. The system was allowed to expand and contract along the a-axis in order to relieve some strain associated

with stacking blocks of sodium that might not be commensurate with tetragonal Na_3SbS_4. One can also see a phase separation (in Figure 4.14) when the atoms moved in the simulation to find a minimum energy configuration that was prefered. It appears as though Na_3SbS_3 and Na_2S also form at the surface of the Na_3SbS_4/Na interface.
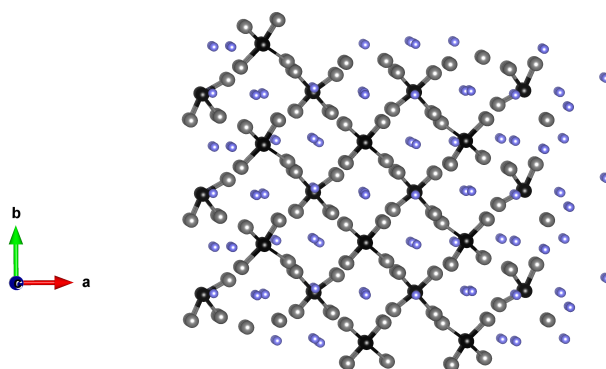

Figure 4.14: Ball-and-stick model of the vc-relaxed (100) surface for Na_3SbS_4 with metallic sodium stacked on top along the a-axis

Again, it is important to note that this interface periodically repeats along the a-axis, so what is seen at the right end of the surface (namely degredation and formation of Na_3SbS_3 and Na_2S, along with Na) is also at the left end of the surface even though it isn't apparent in this picture.

After seeing that Na_2S forms at the interface, we hypothesized that stacking Na_2S on top of Na_3SbS_4 for the interface would stabilize the surface and prevent Na_3SbS_4 from degrading into Na_3SbS_3 and Na_2S.

As one can see, polar Na_2S was stacked on top of Na_3SbS_4 in Figure 4.16, and the system was allowed to "relax" with all three degrees of freedom in Quantum Espresso (meaning the atoms could move freely in any direction to find a minimum energy configuration). It is important to know that the image on the top is the same image that is on the bottom since the images periodically repeat. I showed two surfaces to show how Na_2S is stacked in between the top and bottom surfaces.

One can see that the surface remained intact after the simulation completed in Figure 4.16, but this is far from conclusive evidence that Na_2S acts as a buffer layer and stabilizes the surface of Na_3SbS_4. There is more testing that has been done and testing that needs to be done that includes introducing a nonpolar Na_2S interface at the surface, while allowing the system to contract or expand along the direction of the surface normal
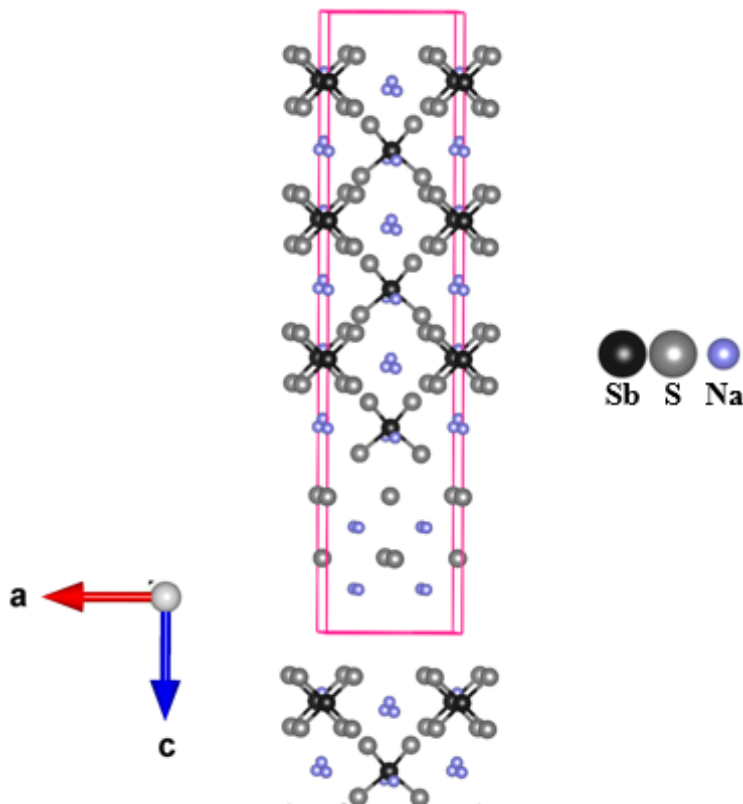
Figure 4.15: Ball-and-stick model of the (001) surface for Na_3SbS_4 Na_2S stacked on top along the c-axis

like what has been done for the Na_3SbS_4/Na interface.

Furthermore, I explored the electronic properties of Na_3SbS_4 by using the Nudged Elastic Band method[20, 21, 22] (or NEB) to obtain the conductivity. I considered a migration mechanism where vacancies for sodium ions were created and allowed to propagate along the a-axis and along the c-axis in Figure 4.1. The mechanism and the activation energy, which is essential when one considers the conductivity of a material (that is an important feature when considering whether or not a material can be used for a solid-state battery because the premise of a battery is to convert chemical energy to electrical energy), is shown in the following figure:

One can see that migration along the a-axis path is the lowest energy path, since the migration energy is 0.05 eV. Banerjee et al.[19] reported the activation energy for Na_3SbS_4 to be 0.2 eV at room temperature based on experiment, so there is some dis-
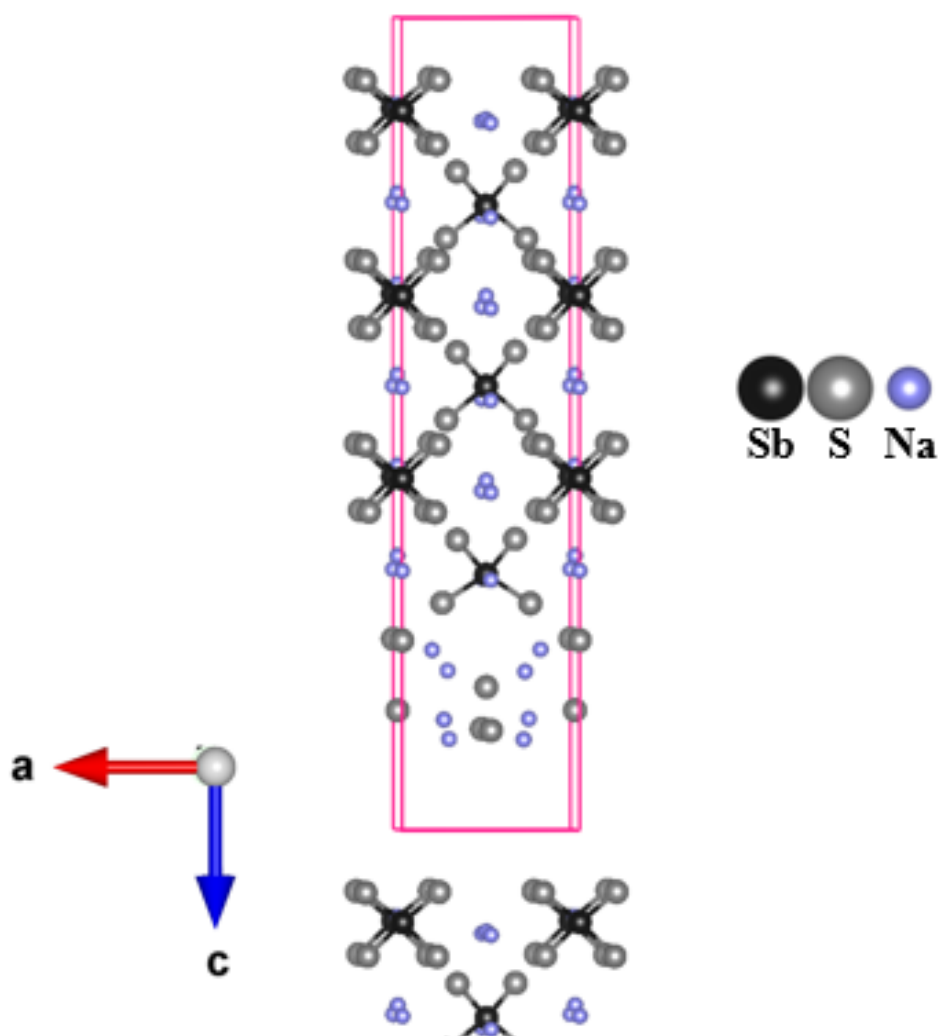
Figure 4.16: Ball-and-stick model of the (001) surface for Na_3SbS_4 Na_2S stacked on top along the c-axis

crepancy with our low temperature model. Since the interface simulations showed the formation of Na_3SbS_3 at the interface, one must consider the conductivity of this material since it is predicted to form after Na_3SbS_4 comes in contact with metallic sodium during cycling of a battery. To model the conductivity of Na_3SbS_3 that forms at the interface of Na_3SbS_4/Na, I modeled the bulk structure for Na_3SbS_3, which is cubic (space group P2$_1$3).

Figure 4.17: Ball-and-stick model of the migration of sodium ions in Na$_3$SbS$_4$
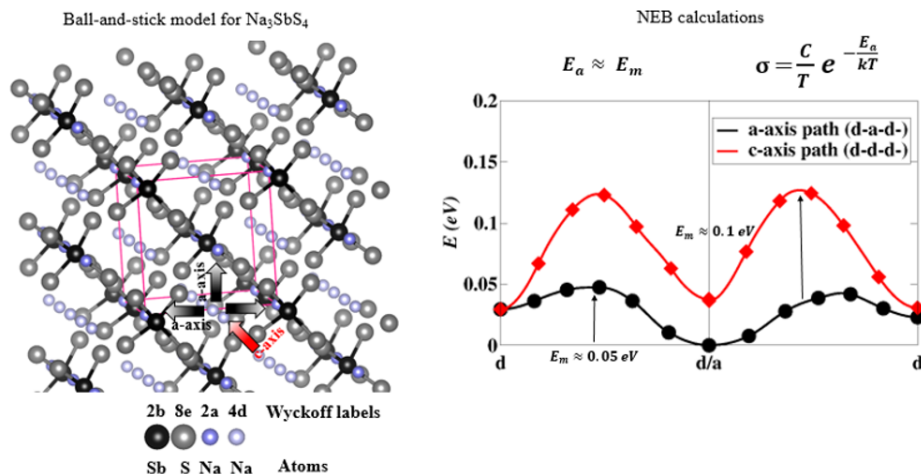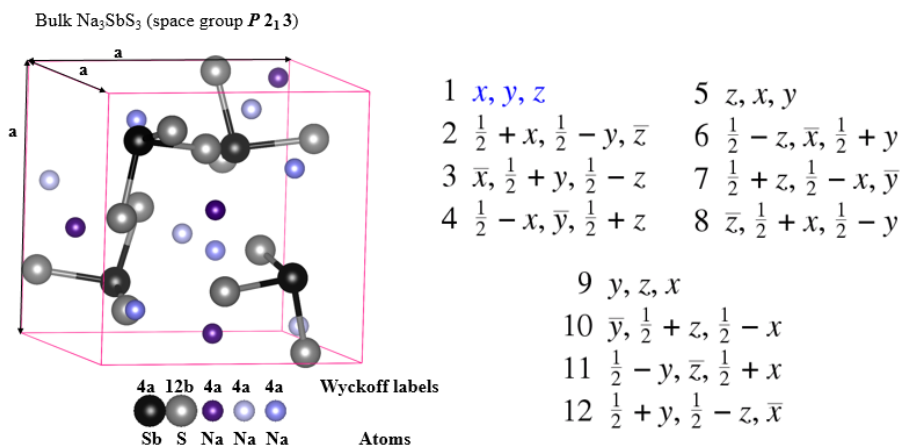

Figure 4.18: Ball-and-stick model of bulk Na$_3$SbS$_3$

Na$_3$SbS$_3$ has three distinct sodium atoms in its structure, but all of them have the same symmetry elements (which is why all three colors have the same Wyckoff label of "a". Also, the structure is cubic so there is only one lattice parameter that is also named "a" in Figure 4.18 (although this "a" is not the same as the Wyckoff label and is just generic).

NEB calculations were performed for pure Na$_3$SbS$_3$, although the pure form did not form at the Na$_3$SbS$_4$/Na interface. There are many paths for sodium ions to flow throughout the crystal (since it is combinatorial), but some knowledge about paths help us reduce the number of plausible ones. Figure 4.19 below shows one path that we believe to

be the lowest based on path length and testing paths that include the third type of sodium (along with the first two types as depicted in the figure). We believe that the minimum
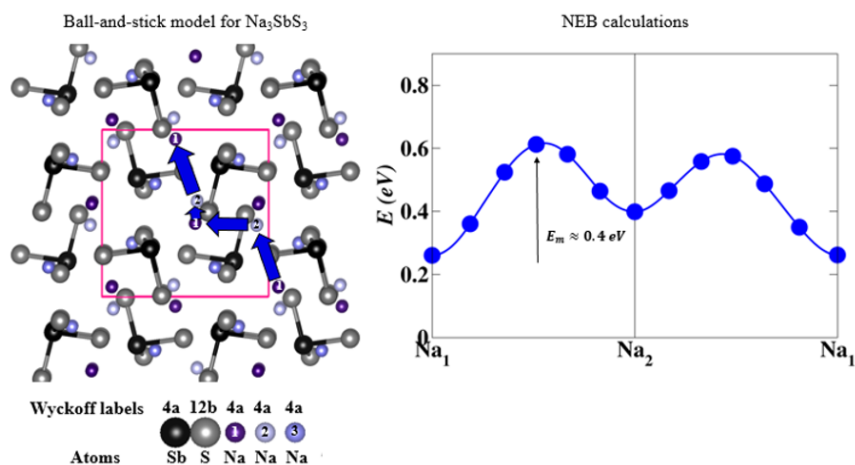
Figure 4.19: Ball-and-stick model of NEB path for bulk Na_3SbS_3

energy path for Na_3SbS_3 only involves migration of the sodium atoms of the first two types because any path that includes the third type of sodium adds approximately .3 eV to the migration energy. Based on the minimum migration energy being 0.4 eV, which is higher than the migration energy for Na_3SbS_4, the barrier is still relatively surmountable so we believe that the battery would still be operational (meaning conductive) even after the formation of the SSEI layer (which is composed of Na_3SbS_3 and Na_2S).

Chapter 5

Conclusions

$Na_4P_2S_6$ and $Li_4P_2S_6$ have key differences in diffusion mechanisms, preferred geometries, and formation energies. The fact that sodium is a larger compound in size could be the reason why ionic diffusion between P_2S_6 units have a lower energy cost than its lithium counterpart, and the Kuhn structure for $Na_4P_2S_6$ could have a higher conductivity than its lithium counterpart based on the fact that there is a .12 eV difference in activation energy for ions moving throughout the crystal. Although the Kuhn structure has more favorable conductivity for $Na_4P_2S_6$ than for $Li_4P_2S_6$, $Li_4P_2S_6$ has a lower heat of formation which means that it is thermodynamically more stable. That means the story for ascertaining how one can exploit the properties of sodium-ion solid-state electrolytes to construct an operational battery with greater or equal benefits to its lithium counterparts is a bit unclear.

Na_3SbS_4 is experimentally known to have a high conductivity, but there are two phases for this compound: a high temperature phase and a low temperature phase. We modeled the conductivity for the low temperature phase, space group $P\bar{4}2_1c$ which is tetragonal, and the activation energy for this phase was 0.05 eV (which is .15 eV lower than what was reported) for ion migration along the a-axis. We also modeled the interface between the solid-state electrolyte, Na_3SbS_4, and the metallic anode, Na, and the simulations show Na_3SbS_4 is reactive towards Na. The intermediates that form at the interface, namely Na_3SbS_3 and Na_2S, form a buffer layer known as the SEI layer, and this layer shows conductivity that suggests that the battery would remain operational if it forms (meaning the activation energy of these materials are comparable to Na_3SbS_4, although it is higher).

Bibliography

[1] The Guardian. Morocco lights the way for Africa on renewable energy, November 2016. https://www.theguardian.com/global-development/2016/nov/17/cop22-host-morocco-lights-way-africa-renewable-energy-2020.

[2] Tim Moynihan. Samsung Finally Reveals Why the Note 7 Kept Exploding, January 2017. https://www.wired.com/2017/01/why-the-samsung-galaxy-note-7-kept-exploding/.

[3] Gerbrand Ceder. Na-ion Battery Materials Design and Discovery. http://ceder.berkeley.edu/research-areas/na-ion-battery-materials-design-and-discovery/.

[4] Giuseppe Grosso and Giuseppe Pastori Parravicini. Solid state physics. In *Solid State Physics (Second Edition)*, pages 1–857. Academic Press, Amsterdam, second edition, 2014.

[5] John P. Perdew and Yue Wang. Accurate and simple analytic representation of the electron-gas correlation energy. *Physical Review B*, 45:13244–13249, 1992.

[6] Paolo Giannozzi and Stefano Baroni and Nicola Bonini and Matteo Calandra and Roberto Car and Carlo Cavazzoni and Davide Ceresoli and Guido L Chiarotti and Matteo Cococcioni and Ismaila Dabo and Andrea Dal Corso and Stefano de Gironcoli and Stefano Fabris and Guido Fratesi and Ralph Gebauer and Uwe Gerstmann and Christos Gougoussis and Anton Kokalj and Michele Lazzeri and Layla Martin-Samos and Nicola Marzari and Francesco Mauri and Riccardo Mazzarello and Stefano Paolini and Alfredo Pasquarello and Lorenzo Paulatto and Carlo Sbraccia and Sandro Scandolo and Gabriele Sclauzero and Ari P Seitsonen and Alexander Smogunov and Paolo Umari

and Renata M Wentzcovitch. Quantum espresso: a modular and open-source software project for quantum simulations of materials. *Journal of Physics: Condensed Matter*, 21(39):395502 (19pp), 2009.

[7] P. E. Blöchl. Projector augmented-wave method. *Phys. Rev. B*, 50:17953–17979, Dec 1994.

[8] N.A.W. Holzwarth, A.R. Tackett, and G.E. Matthews. A projector augmented wave (paw) code for electronic structure calculations, part i: atompaw for generating atom-centered functions. *Computer Physics Communications*, 135(3):329 – 347, 2001.

[9] Woody Austin, Grey Ballard, and Tamara G. Kolda. Parallel tensor compression for large-scale scientific data. In *Proceedings of the 30th IEEE International Parallel and Distributed Processing Symposium*, pages 912–922, May 2016.

[10] Tamara Kolda and Brett Bader. Tensor Decompositions and Applications, November 2007.

[11] Volker Strassen. Gaussian Elimination is not Optimal. *Numerische Mathematik*, 13:354–356, August 1969.

[12] Harald Prokop. *Cache-Oblivious Algorithms*. PhD thesis, Massachusetts Institute of Technology, June 1999.

[13] Grey Ballard, James Demmel, Olga Holtz, and Oded Schwartz. Communication costs of strassen's matrix multiplication. *Communications of the ACM*, 57(2):107–114, February 2014.

[14] R. Mercier, J. P. Malugani, B. Fahys, J. Douglade, and G. Robert. Synthese, structure cristalline at analyse vibrationnelle de l'hexathiohypodiphosphate de lithium $Li_4P_2S_6$. *Journal of Solid State Chemistry*, 43:151–162, 1982.

[15] Alexander Kuhn, Roland Eger, Jrgen Nuss, and Bettina V. Lotsch. Synthesis and structural characterization of the alkali thiophosphates $Na_2P_2S_6$, $Na_4P_2S_6$, $K_4P_2S_6$, and $Rb_4P_2S_6$. *Zeitschrift für anorganische und allgemeine Chemie*, 640(5):689–692, April 2014.

[16] Zachary D. Hood, Cameron Kates, Melanie Kirkham, Shiba Adhikari, Chengdu Liang, and N.A.W. Holzwarth. Structural and electrolyte properties of li4p2s6. *Solid State Ionics*, 284:61 – 70, 2016.

[17] Hui Wang, Yan Chen, Zachary D. Hood, Gayatri Sahu, Amaresh Samuthira Pandian, Jong Kahk Keum, Ke An, and Chengdu Liang. An air-stable na3sbs4 superionic conductor prepared by a rapid and economic synthetic procedure. *Angewandte Chemie International Edition*, 55(30):8551–8555, 2016.

[18] Long Zhang, Dechao Zhang, Kun Yang, Xinlin Yan, Limin Wang, Jianli Mi, Bo Xu, and Yueming Li. Vacancy-contained tetragonal na3sbs4 superionic conductor. *Advanced Science*, 3(10):1600089–n/a, 2016. 1600089.

[19] Abhik Banerjee, Kern Ho Park, Jongwook W. Heo, Young Jin Nam, Chang Ki Moon, Seung M. Oh, Seung-Tae Hong, and Yoon Seok Jung. Na3sbs4: A solution process-able sodium superionic conductor for all-solid-state sodium-ion batteries. *Angewandte Chemie International Edition*, 55(33):9634–9638, 2016.

[20] H. Jónsson, G. Mills, and K. W. Jacobsen. Nudged elastic band method for finding minimum energy paths of transitions. In B. J. Berne, G. Ciccotti, and D. F. Coker, editors, *Classical and Quantum Dynamics in Condensed Phase Simulations*, pages 385–404. World Scientific, Singapore, 1998.

[21] Graeme Henkelman, Blas P. Uberuaga, and Hannes Jónsson. A climbing image nudged elastic band method for finding saddle points and minimum energy paths. *Journal of Chemical Physics*, 113:9901–9904, 2000.

[22] Graeme Henkelman and Hannes Jónsson. Improved tangent estimate in the nudged elastic band method for finding minimum energy paths and saddle points. *Journal of Chemical Physics*, 113:9978–9985, 2000.

Part I

Curriculum Vitae

Curriculum Vitae

Larry Edward Rush Jr.

304-777-0558 | lrush88@gmail.com

Summary

I am a M.S. physics graduate who is primarily interested in big data analytics and machine learning/artificial intelligence. I have experience developing algorithms for K-Means clustering analysis on data, researching numerical algorithms for tensor decomposition in Density Functional Theory simulations, and performing analysis on data using Bayesian inference. I primarily code in C/C++ or MATLAB.

Skills

C/C++, MATLAB, Linux, Algorithms, Communication, Adaptability

Education

Wake Forest University
Winston-Salem, NC
Master's Graduate Student in Physics
August 2014- May 2017
• Sigma Pi Sigma inductee (The physics honor society)
• Society of Physics Students (SPS) volunteer
• North Carolina Science Olympiad volunteer
West Virginia University
Morgantown, WV
BS in Physics (Emphasis in Biophysics), B.S. in Mathematics
August 2010- August 2012
West Virginia University,
Morgantown, WV
B.S. in Chemistry, Physics Minor, Mathematics Minor
August 2006- May 2010
• Dean's List Spring 2008
• Honors College (2006-2008)
• NASA Space Grant Fellowship Recipient

Professional Development

APS March Meeting (2017), New Orleans, LA. Presented "Computational Study of Ideal Electrolyte/Anode Interface for Na_3SbS_4/Na".

APS 2017 Joint Graduate Education and Bridge Program Conference, College Park, MD. Presented "Computational Study of Ideal Electrolyte/Anode Interface for Na_3SbS_4/Na".

Rush, Larry; Holzwarth, Natalie. "First principles investigation of the structural and electrochemical properties of $Na_4P_2S_6$ and $Li_4P_2S_6$." *Solid State Ionics,* 284 (2016): 45-50. Web. 7 Jan. 2016.

APS March Meeting (2016), Baltimore, MD. Presented "First Principles Investigation of the Geometrical and Electrochemical Properties of $Na_4P_2S_6$ and $Li_4P_2S_6$".

APS National Mentoring Community (NMC) Conference (2015), Miami, FL. Presented "Investigation of the structural properties of $Na_4P_2S_6$ and $Li_4P_2S_6$".

<u>Experience</u>

Theoretical Condensed Matter Physicist
August 2014- present
Wake Forest University
Winston-Salem, NC

* Applied First Principles to solid-state battery technology in Dr. Natalie Holzwarth's Computational Materials Group
* Hypothesized the use of algorithms employed in Machine Learning to improve the quality of data-sets obtained for ATOMPAW code
* Critiqued and contributed to the conception and development of rationale for various projects during weekly group discussions (including implementing Tucker decomposition of large data to get speed-up)
* Analyzed 10GB-50GB of data generated by Quantum Espresso to investigate the interface properties of solid-state materials with Linux/Gnuplot

Systems Engineer
April 2014- August 2014
ManTech Corporation
Lexington Park, MD

* Ran simulations for Naval aircraft carriers that was based on physics